INSTITUTE OF PHYSICS PUBLISHING JOURNAL OF PHYSICS: CONDENSED MATTER

J. Phys.: Condens. Matter **16** (2004) R829–R858 PII: S0953-8984(04)58969-5

TOPICAL REVIEW

Zinc oxide nanostructures: growth, properties and applications

Zhong Lin Wang

School of Materials Science and Engineering, Georgia Institute of Technology, Atlanta, GA 30332-0245, USA

E-mail: zhong.wang@mse.gatech.edu

Received 8 April 2004
Published 11 June 2004
Online at stacks.iop.org/JPhysCM/16/R829
doi:10.1088/0953-8984/16/25/R01

Abstract

Zinc oxide is a unique material that exhibits semiconducting and piezoelectric dual properties. Using a solid–vapour phase thermal sublimation technique, nanocombs, nanorings, nanohelixes/nanosprings, nanobelts, nanowires and nanocages of ZnO have been synthesized under specific growth conditions. These unique nanostructures unambiguously demonstrate that ZnO probably has the richest family of nanostructures among all materials, both in structures and in properties. The nanostructures could have novel applications in optoelectronics, sensors, transducers and biomedical sciences. This article reviews the various nanostructures of ZnO grown by the solid–vapour phase technique and their corresponding growth mechanisms. The application of ZnO nanobelts as nanosensors, nanocantilevers, field effect transistors and nanoresonators is demonstrated.

(Some figures in this article are in colour only in the electronic version)

Contents

1. Introduction

Nanostructured ZnO materials have received broad attention due to their distinguished performance in electronics, optics and photonics. From the 1960s, synthesis of ZnO thin films has been an active field because of their applications as sensors, transducers and catalysts. In the last few decades, especially since the nanotechnology initiative led by the US, study of one-dimensional (1D) materials has become a leading edge in nanoscience and nanotechnology. With reduction in size, novel electrical, mechanical, chemical and optical properties are introduced, which are largely believed to be the result of surface and quantum confinement effects. Nanowire-like structures are the ideal system for studying the transport process in one-dimensionally (1D) confined objects, which are of benefit not only for understanding the fundamental phenomena in low dimensional systems, but also for developing new generation nanodevices with high performance.

ZnO is a key technological material. The lack of a centre of symmetry in wurtzite, combined with large electromechanical coupling, results in strong piezoelectric and pyroelectric properties and the consequent use of ZnO in mechanical actuators and piezoelectric sensors. In addition, ZnO is a wide band-gap (3.37 eV) compound semiconductor that is suitable for short wavelength optoelectronic applications. The high exciton binding energy (60 meV) in ZnO crystal can ensure efficient excitonic emission at room temperature and room temperature ultraviolet (UV) luminescence has been reported in disordered nanoparticles and thin films. ZnO is transparent to visible light and can be made highly conductive by doping.

ZnO is a versatile functional material that has a diverse group of growth morphologies, such as nanocombs, nanorings, nanohelixes/nanosprings, nanobelts, nanowires and nanocages. The objective of this article is to review the unique nanostructures that have been grown for ZnO and their corresponding growth mechanisms. The potential applications and novel nanodevices demonstrated for ZnO and SnO_2 nanostructures will be reviewed.

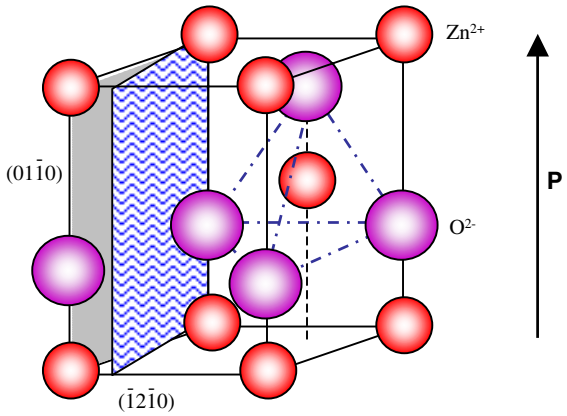

Figure 1. The wurtzite structure model of ZnO. The tetrahedral coordination of Zn–O is shown.

2. Crystal and surface structure of ZnO

Wurtzite zinc oxide has a hexagonal structure (space group $C6mc$) with lattice parameters $a = 0.3296$ and $c = 0.52065$ nm. The structure of ZnO can be simply described as a number of alternating planes composed of tetrahedrally coordinated O^{2-} and Zn^{2+} ions, stacked alternately along the c-axis (figure 1). The tetrahedral coordination in ZnO results in non-central symmetric structure and consequently piezoelectricity and pyroelectricity. Another important characteristic of ZnO is polar surfaces. The most common polar surface is the basal plane. The oppositely charged ions produce positively charged Zn-(0001) and negatively charged O-(000$\bar{1}$) surfaces, resulting in a normal dipole moment and spontaneous polarization along the c-axis as well as a divergence in surface energy. To maintain a stable structure, the polar surfaces generally have facets or exhibit massive surface reconstructions, but ZnO-$\pm$(0001) are exceptions: they are atomically flat, stable and without reconstruction [1, 2]. Efforts to understand the superior stability of the ZnO $\pm$(0001) polar surfaces are at the forefront of research in today's surface physics [3–6]. The other two most commonly observed facets for ZnO are {2$\bar{1}\bar{1}$0} and {01$\bar{1}$0}, which are non-polar surfaces and have lower energy than the {0001} facets.

3. Typical growth structures of ZnO

Structurally, ZnO has three types of fast growth directions: ⟨2$\bar{1}\bar{1}$0⟩ ($\pm$[2$\bar{1}\bar{1}$0], $\pm$[$\bar{1}$2$\bar{1}$0], $\pm$[$\bar{1}\bar{1}$20]); ⟨01$\bar{1}$0⟩ ($\pm$[01$\bar{1}$0], $\pm$[10$\bar{1}$0], $\pm$[1$\bar{1}$00]); and $\pm$[0001]. Together with the polar surfaces due to atomic terminations, ZnO exhibits a wide range of novel structures that can be grown by tuning the growth rates along these directions. One of the most profound factors determining the morphology involves the relative surface activities of various growth facets under given conditions. Macroscopically, a crystal has different kinetic parameters for different crystal planes, which are emphasized under controlled growth conditions. Thus, after an initial period of nucleation and incubation, a crystallite will commonly develop into a three-dimensional object with well-defined, low index crystallographic faces. Figures 2(a)–(c) show a few typical growth morphologies of 1D nanostructures for ZnO. These structures tend to maximize the areas of the {2$\bar{1}\bar{1}$0} and {01$\bar{1}$0} facets because of the lower energy. The morphology shown in figure 2(d) is dominated by the polar surfaces, which can be grown

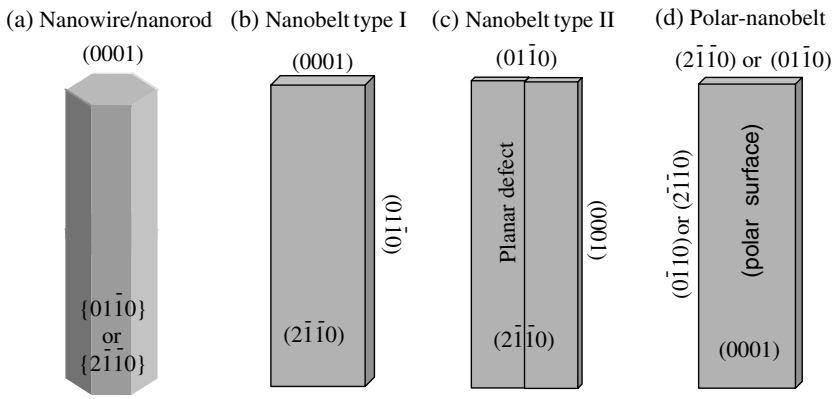

Figure 2. Typical growth morphologies of one-dimensional ZnO nanostructures and the corresponding facets.

by introducing planar defects parallel to the polar surfaces [7]. Planar defects and twins are observed occasionally parallel to the (0001) plane, but dislocations are rarely seen.

4. Synthesis techniques

The oxide nanostructures to be reviewed in this paper were synthesized by a solid–vapour process. In principle, the thermal evaporation technique is a simple process in which condensed or powder source material(s) is/are vaporized at elevating temperature and then the resultant vapour phase(s) condense(s) under certain conditions (temperature, pressure, atmosphere, substrate etc) to form the desired product(s). The processes are usually carried out in a horizontal tube furnace, as shown in figure 3, which is composed of a horizontal tube furnace, an alumina tube, a rotary pump system and a gas supply and control system. A viewing window is set up at the left end of the alumina tube, which is used to monitor the growth process. The right-hand end of the alumina tube is connected to the rotary pump. Both ends are sealed by rubber O-rings. The ultimate vacuum for this configuration is $\sim 2 \times 10^{-3}$ Torr. The carrying gas comes in from the left end of the alumina tube and is pumped out at the right end. The source material(s) is/are loaded on an alumina boat and positioned at the centre of the alumina tube, where the temperature is the highest. Alumina substrates were placed downstream for collecting growth products. This simple set-up can achieve high control of the final product.

There are several processing parameters such as temperature, pressure, carrier gas (including gas species and its flow rate), substrate and evaporation time period, which can be controlled and need to be selected properly before and/or during the thermal vaporization [8]. The source temperature selection mainly depends on the volatility of the source material(s). Usually, it is slightly lower than the melting point of the source material. The pressure is determined according to the evaporation rate or vapour pressure of the source material(s). The substrate temperature usually drops with the distance of its location from the position of the source material(s). *The local temperature determines the type of product that will be obtained*. It is also noted that the thermal evaporation process is very sensitive to the concentration of oxygen in the growth system. Oxygen influences not only the volatility of the source material(s) and the stoichiometry of the vapour phase, but also the formation of the product(s). In the present study, after evacuating the alumina tube to $\sim 2 \times 10^{-3}$ Torr, thermal vaporization was conducted at a designed heating rate and at a pressure of 200–600 Torr and Ar carrier gas at

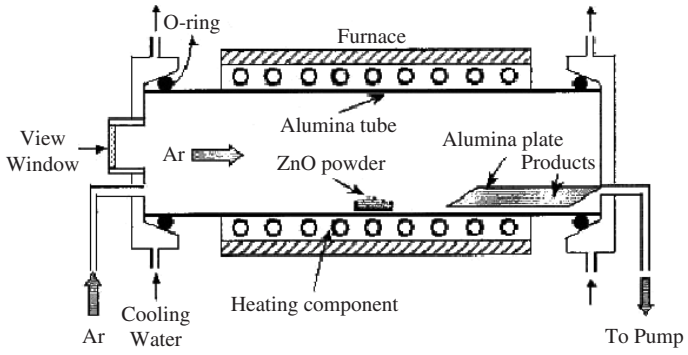

Figure 3. A schematic diagram of the experimental apparatus for growth of oxides nanostructures by the solid–vapour phase process.

50 sccm (standard cubic centimetres per minute). The on and off times as well as the duration of inlet of the carrier gas could greatly affect the growth kinetics.

The as-deposited products were characterized and analysed by means of x-ray diffraction (XRD) (Philips PW 1800 with Cu Kα radiation), scanning electron microscopy (SEM) (LEO 1530 FEG), transmission electron microscopy (TEM) (Hitachi HF-2000 FEG at 200 kV and JEOL 4000EX high resolution TEM (HRTEM) at 400 kV) and energy dispersive x-ray spectroscopy (EDS).

5. Nanostructures and the growth processes

The different surface structures of ZnO could induce anisotropic growth. Under thermodynamic equilibrium conditions, the facet with higher surface energy is usually small in area, while the lower energy facets are larger. Specifically, in the ZnO growth, the highest growth rate is along the *c*-axis and the large facets are usually $\{01\bar{1}0\}$ and $\{2\bar{1}\bar{1}0\}$. By controlling the growth kinetics, it is possible to change the growth behaviour of ZnO nanobelts. Here, we received various ZnO nanostructures by means of the controllable synthesized parameters, such as deposition temperatures and pressures as well as carrier gas flux. The ZnO nanostructures presented here include nanorods, ultralong nanobelts with diverse facets, nanocombs, branched hierarchical structures, nanohelixes and nanorings.

5.1. Nanorods

Growth of 1D nanostructure usually follows the vapour–liquid–solid (VLS) approach, in which a liquid alloy droplet composed of a metal catalyst component (such as Au, Fe) and a nanowire component (such as Si, III–V compound, II–V compound, oxide) is first formed under the reaction conditions. The metal catalyst can be rationally chosen from the phase diagram by identifying metals in which the nanowire component elements are soluble in the liquid phase but do not form solid compounds more stable than the desired nanowire phase. For the 1D ZnO nanowires grown via a VLS process, the commonly used catalyst for ZnO is Au [9]. The liquid droplet serves as a preferential site for absorption of gas phase reactant and, when supersaturated, the nucleation site for crystallization. Nanowire growth begins after the liquid becomes supersaturated in reactant materials and continues as long as the catalyst alloy remains in a liquid state and the reactant is available. During growth, the catalyst droplet directs the nanowire's growth direction and defines the diameter of the nanowire. Ultimately, the growth

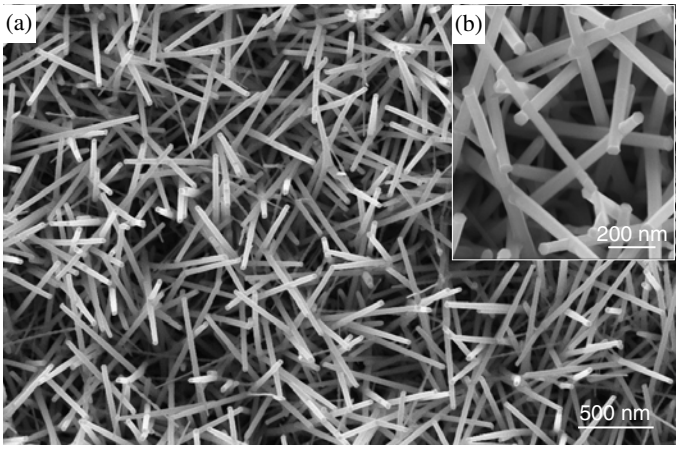

Figure 4. (a) ZnO nanorods grown using gold as a catalyst. (b) An enlarged image of the nanorods, showing gold particles at the tips (courtesy of Dr X Y Kong).

terminates when the temperature is below the eutectic temperature of the catalyst alloy or the reactant is no longer available. As a result, a nanowire obtained from the VLS process typically has a solid catalyst nanoparticle at its tip with a diameter comparable to that of the connected nanowires. Thus, one can usually determine whether the nanowire growth was governed by a VLS process from whether there is a catalyst particle present at one end of the nanowire.

The VLS crystal growth mechanism was first proposed by Wagner and Ellis [10] in 1964 for Si whisker growth, in which Si whiskers with diameters of up to the micrometre scale were grown by hydrogen reduction of $SiCl_4$ with the presence of Au, Pt, Ag, Pd, Cu and Ni as the catalysts. Westwater *et al* [11] and Lieber *et al* [12] then developed this mechanism and successfully prepared nanometre scale Si wires by pyrolysis of SiH_4 with Au as the catalyst and laser ablation of $Si_{0.95}Fe_{0.05}$ targets, respectively.

Figure 4 shows an SEM image of uniform ZnO nanorods/nanowires grown using Au catalyst on a polycrystalline alumina substrate. The nanorods show no alignment and are dispersively distributed, but their diameters and lengths are rather uniform, as defined by the size of the Au catalyst. The catalyst particles locate at the tips of the nanowires, as can be seen in the enlarged image. The nanorods grow along [0001] and their side surfaces are enclosed by $\{2\bar{1}\bar{1}0\}$.

Recently, we have found that Sn can also be an effective catalyst for growing ZnO nanorods [13]. Using the epitaxial growth of ZnO nanorods on ZnO crystal, aligned nanorods have been grown (figure 5) [14]. In this case, the growth direction of the nanorods is led by the Sn catalyst and the epitaxial orientation is defined by the substrate that determines the aligned growth. The nanorods are also aligned in orientation because they tend to take the least mismatch orientation on the substrate, to reduce the interface mismatch energy. The choice of substrate is important for the epitaxial growth. One must consider the crystallographic structure as well as the surfaces to be used for the growth. We have found recently that the atomic termination and charge status of the substrate can strongly affect the morphology of the grown nanorods [15]. The nanorods growing out of Zn-terminated (0001) ZnO substrates are very different from those grown out of the oxygen-terminated $(000\bar{1})$ ZnO substrates although the same type of Sn catalyst was used.

The growth morphology of the ZnO nanorods is also affected by the geometrical shape of the substrate. Figure 6 shows aligned nanorods grown on a cylindrical shape substrate.

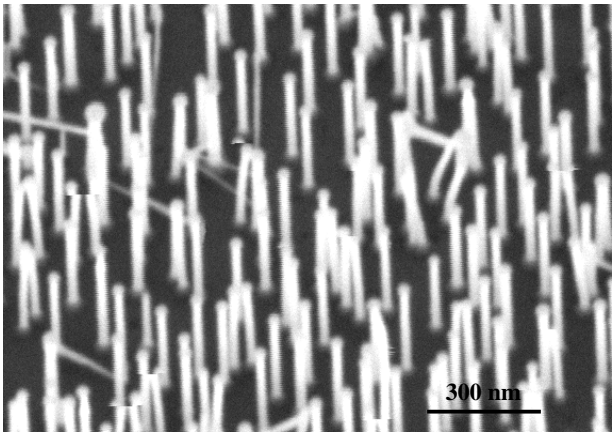

Figure 5. Aligned ZnO nanorods/nanowires epitaxially grown on ZnO substrate using Sn as a catalyst (image courtesy of P X Gao) [14].

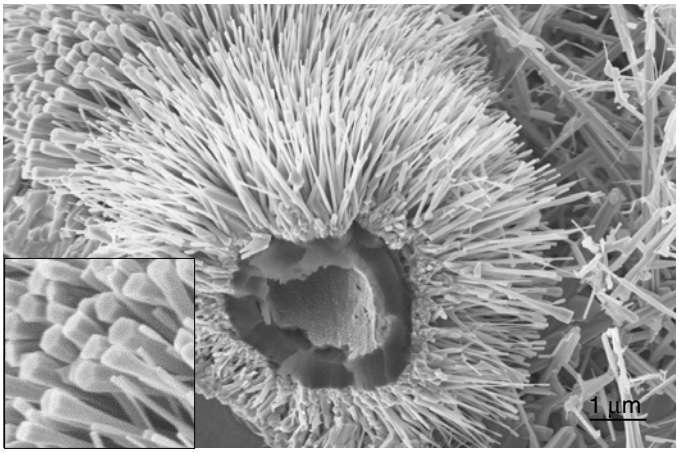

Figure 6. ZnO nanowires and nanonails grown following the cylindrical shape of a substrate (courtesy of Dr X Y Kong).

The nanorods grow along [0001], but the area of the cross section increases radially with the increase of the radius, which can be apparently seen through the enlarged SEM image. The nanorods have a 'nail' shape [16].

5.2. Nanobelts

Nanobelts are nanowires that have a well-defined geometrical shape and side surfaces. Nanobelts of ZnO are usually grown [17] by sublimation of ZnO powder without introducing a catalyst. Figure 7 shows a TEM image of ZnO nanobelts, displaying different morphologies from the nanowires and nanorods. Each nanobelt has a uniform width along its entire length and the typical widths of the nanobelts are in the range of 50 to 300 nm and thicknesses are 10 to 30 nm. No particle was observed at the ends of the nanobelts. A ripple-like contrast that appeared in the TEM image is due to strain resulting from the bending of the belt. The nanobelt grows along $[01\bar{1}0]$, with top and bottom flat surfaces $\pm(2\bar{1}\bar{1}0)$ and side surfaces $\pm(0001)$.

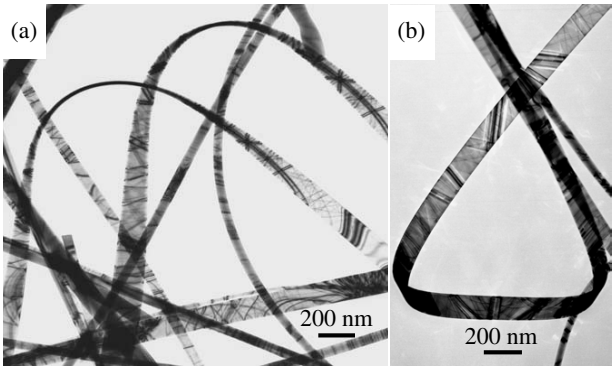

Figure 7. TEM images of the as-synthesized ZnO nanobelts, showing uniform morphology (image courtesy of Dr Z W Pan) [17].

The cross section of the nanobelt is rectangular, with typical thickness and width-to-thickness ratios of ∼5 to 10.

5.3. Ultranarrow nanobelts

For investigation of the quantum confinement effect, nanobelts of small sizes are required. We have recently grown ultrasmall nanobelts using a novel catalyst [18]. In the experimental process, a silicon substrate was first cleaned by a 2:1 mixture (by volume) of H_2SO_4 (98%) and H_2O_2. Instead of using dispersive nanoparticles as the catalyst for seeded growth, a uniform thin film (∼10 nm) of tin was coated on the silicon substrate. A thermal evaporator with a quartz crystal thickness monitor was used to obtain the exact tin film thickness. For nanowire growth, an equimolar mixture of ZnO powder and graphite powder was ground and loaded into an alumina boat.

The ZnO nanobelts produced by the tin film catalyst are rather narrow, thin and uniform (figure 8(a)). The electron diffraction pattern and high resolution TEM image show that the nanobelts grow along [0001]; the top surfaces are $(2\bar{1}\bar{1}0)$ and the side surfaces are $(0\bar{1}10)$. Measuring over 120 nanobelts from randomly recorded TEM images shows that the average diameter of the nanobelts is 5.5 nm with a standard deviation of ±1.5 nm; most nanobelts are in the range of 4–7 nm, indicating very good size uniformity.

To examine the size induced quantum effect in the ultrathin ZnO nanobelts, photoluminescence (PL) measurements were performed at room temperature using a Xe lamp with an excitation wavelength of 330 nm (figure 8(b)). In comparison to the PL from nanobelts of an average width of ∼200 nm, the 6 nm nanobelts have a 14 nm shift in the emission peak, which possibly indicates a quantum effect due to the reduced size of the nanobelts.

The optical properties of ZnO are sensitive to the doping. By varying the doping level of Ga in ZnO nanotips, their photoluminescence intensity has been tuned [19]. This was attributed to donor-related impurity emission and the results correspond well to the current–voltage characteristics of the ZnO nanotips.

5.4. Hierarchical nanostructures

Modifying the composition of the source materials can drastically change the morphology of the grown oxide nanostructure. We used a mixture of ZnO and SnO_2 powders in a weight ratio of 1:1 as the source material to grow a complex ZnO nanostructure [13].

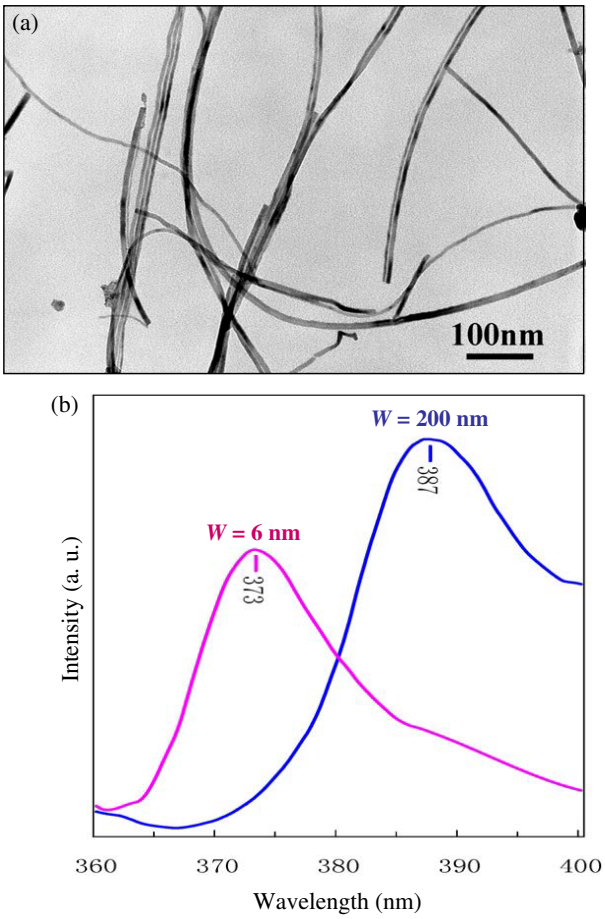

Figure 8. (a) Controlled synthesis of 6 nm wide ZnO nanobelts. (b) Photoluminescence spectra recorded from ZnO nanobelts with widths of 200 and 6 nm, respectively, showing a blue-shift with a reduction in nanobelt size (image courtesy of X D Wang) [18].

Figure 9(a) shows a low magnification SEM image of the as-synthesized products with a uniform feature consisting of sets of central axial nanowires, surrounded by radically distributed nanobranches. It is known that SnO_2 decomposes into Sn and O_2 at high temperature; thus, the growth of the nanowire–nanoribbon junction arrays is the result of a VLS growth process, in which the Sn catalyst particles are responsible for initiating and leading the growth of ZnO nanowires and nanoribbons. The growth of the novel structure presented here can be separated into two stages. The first stage is a fast growth of the ZnO axial nanowire along [0001]. The growth rate is so high that a slow increase in the size of the Sn droplet has little influence on the diameter of the nanowire; thus the axial nanowire has a fairly uniform shape along the growth direction. The second stage of the growth is the nucleation and epitaxial growth of the nanoribbons due to the arrival of the tiny Sn droplets on the ZnO nanowire surface (figure 9(b)). This stage is much slower than the first stage because the lengths of the nanoribbons are uniform and much shorter than that of the nanowire. The ZnO nanowire is likely to have a hexagonal cross section bounded by $\pm(10\bar{1}0)$, $\pm(01\bar{1}0)$ and $\pm(\bar{1}100)$, which are six crystallographically equivalent planes. The Sn liquid droplets deposited on the ZnO nanowire lead to the simultaneous growth of ZnO nanoribbons along the six growth directions:

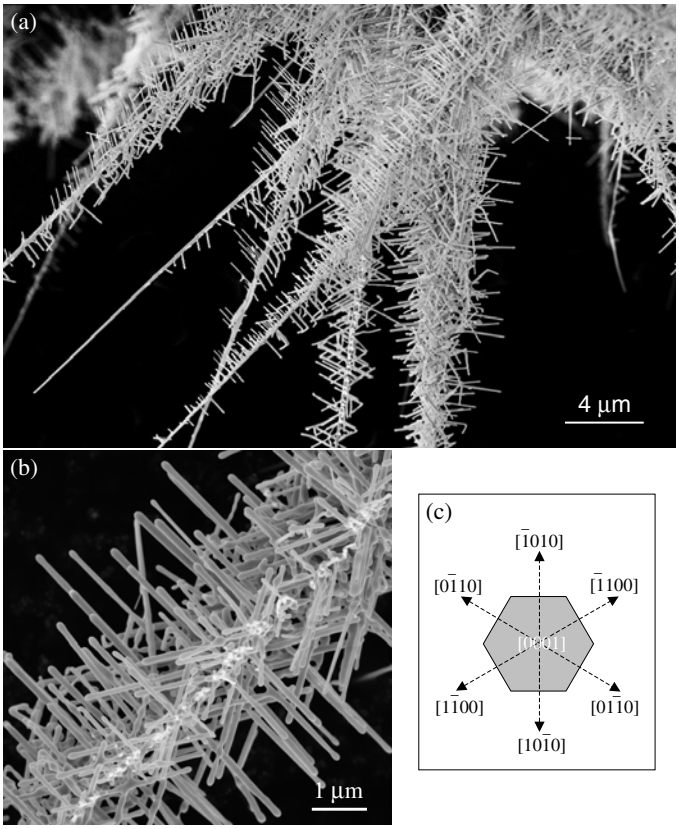

Figure 9. ((a), (b)) SEM images of the hierarchical ZnO nanowire junction arrays (image courtesy of Dr X Y Kong). (c) The growth model of the hierarchical structure.

$\pm[10\bar{1}0]$, $\pm[0\bar{1}10]$ and $\pm[\bar{1}100]$ (figure 9(c)). The angle between the two adjacent growth directions is 60°, resulting in a sixfold symmetric distribution of the nanoribbons around the nanowire.

5.5. Nanocombs and nanosaws

'Comb-like' structures of ZnO have been reported [20], but the mechanism that drives the growth was not elaborated until recently. The comb structures we have received (figure 10) have comb teeth growing along [0001], the top/bottom surfaces being $\pm(01\bar{1}0)$ and the side surfaces $\pm(2\bar{1}\bar{1}0)$. Using convergent beam electron diffraction (CBED) [21], which relies on the dynamic scattering effect and is an effective technique for determining the polarity of wurtzite structure, we have found that the comb structure is an asymmetric growth along Zn-[0001] [22]. The positively charged Zn(0001) surface is chemically active and the negatively charged O-$(000\bar{1})$ surface is relatively inert, resulting in growth of long fingers along [0001]. Using HRTEM, we found that the Zn-terminated (0001) surface has tiny Zn clusters, which could lead to *self-catalysed growth* [22] without the presence of foreign catalyst [22]. The chemically inactive $(000\bar{1})$ surface typically does not grow nanobelt structure.

The anisotropic growth appears to be a common characteristic for the wurtzite family. Similar sawtooth growth has been observed for ZnS [23] and CdSe [24] and it is induced by the Zn- and Cd-terminated (0001) surfaces, respectively.

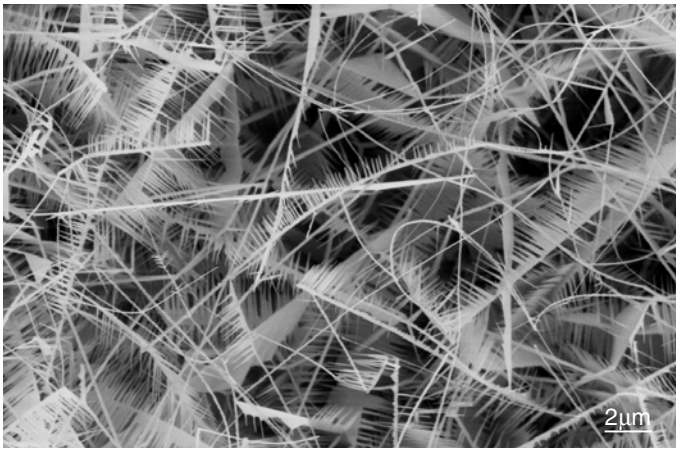

Figure 10. An SEM image of 'comb-like' cantilever arrays of ZnO, which are the result of surface polarization induced growth due to the chemically active (0001) Zn (image courtesy of Dr X Y Kong) [22].

5.6. Nanosprings and nanospirals

Due to differences in surface energies among (0001), $\{01\bar{1}0\}$ and $\{2\bar{1}\bar{1}0\}$, free-standing nanobelts and nanowires of ZnO are usually dominated by the lower energy, non-polar surfaces such as $\{01\bar{1}0\}$ and $\{2\bar{1}\bar{1}0\}$. Recently, by introducing doping, such as that of In and/or Li, ZnO nanobelts dominated by the (0001) polar surfaces have been grown [25]. The nanobelt grows along $[2\bar{1}\bar{1}0]$ (the *a*-axis), with its top/bottom large surface $\pm(0001)$ and the side surfaces $\pm(01\bar{1}0)$. Due to the small thickness of 5–20 nm and large aspect ratio of ∼1:4, the flexibility and toughness of the nanobelts are extremely high. A polar surface dominated nanobelt can be approximated as a capacitor with two parallel charged plates (figure 11(a)). The polar nanobelt tends to roll over into an enclosed ring to reduce the electrostatic energy (figure 11(b)). A spiral shape is also possible for reducing the electrostatic energy (figure 11(c)) [26]. The formation of the nanorings and nanohelixes can be understood from the nature of the polar surfaces [25]. If the surface charges are uncompensated during the growth, the spontaneous polarization induces electrostatic energy due to the dipole moment, but rolling up to form a circular ring would minimize or neutralize the overall dipole moment, reducing the electrostatic energy. On the other hand, bending of the nanobelt produces elastic energy. The stable shape of the nanobelt is determined by the minimization of the total energy contributed by spontaneous polarization and elasticity.

If the nanobelt is rolled loop by loop, the repulsive force between the charged surfaces stretches the nanospring, while the elastic deformation force pulls the loops together; the balance between the two forms a nanospring that has elasticity (figure 11(d)). The nanospring has a uniform shape with radius ∼500–800 nm and evenly distributed pitches. Each is made of a uniformly deformed single-crystal ZnO nanobelt.

5.7. Seamless nanorings

By adjusting the raw materials with the introduction of impurities, such as indium, we have synthesized a nanoring structure of ZnO (figure 12(a)) [27]. The TEM image indicates that the nanoring is a single-crystal entity with circular shape. The single-crystal structure referred to

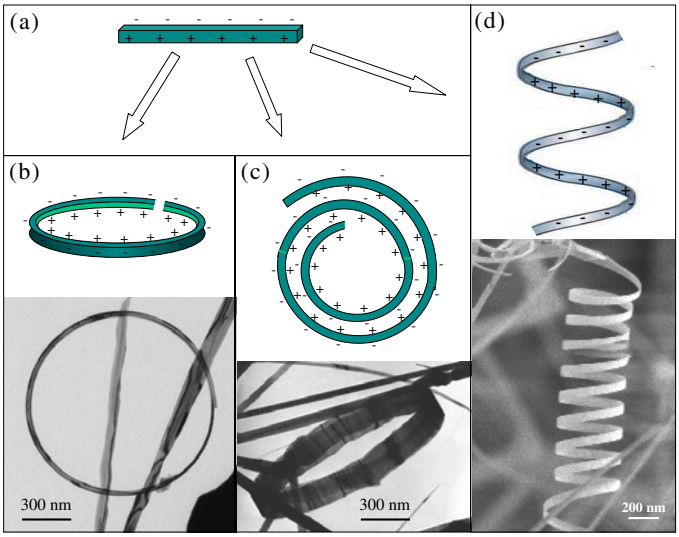

Figure 11. (a) The model of a polar nanobelt. Polar surface induced formation of (b) a nanoring, (c) a nanospiral and (d) nanohelixes of ZnO and their formation processes (see the text).

here means a complete nanoring that is made of a single-crystalline ribbon bent evenly at the curvature of the nanoring. Although the radius of the ring is large, its thickness is only ∼10 nm (figure 12(b)). The nanoring is a uniformly deformed single crystal along its circumference, and is made of a loop-by-loop coaxial, uni-radius, epitaxial coiling of a nanobelt, as can be seen through the contrast displayed by the dark-field TEM image (figure 12(c)) [27].

The growth of the nanoring structures can be understood from the polar surfaces of the ZnO nanobelt. The polar nanobelt, which is the building block of the nanoring, grows along $[10\bar{1}0]$, with side surfaces $\pm(1\bar{2}10)$ and top/bottom surfaces $\pm(0001)$, and has a typical width of ∼15 nm and thickness ∼10 nm. The nanobelt has polar charges on its top and bottom surfaces (figure 13(a)). If the surface charges are uncompensated during growth, the nanobelt may tend to fold itself as its length gets longer to minimize the area of the polar surface. One possible approach is to interface the positively charged Zn-(0001) plane (top surface) with the negatively charged O-(0001) plane (bottom surface), resulting in neutralization of the local polar charges and the reduced surface area, thus forming a loop with an overlapped end (figure 13(b)). This type of folding is at 90° with respect to the folding direction for forming the nanospring or nanospiral (see figure 11), possibly due to the difference in aspect ratio of the nanobelts and relative size of the polar surfaces. The radius of the loop may be determined by the initial folding of the nanobelt in the initial growth, but the size of the loop cannot be too small to reduce the elastic deformation energy. The total energy involved in the process comes from polar charges, the surface area and elastic deformation. The long range electrostatic interaction is likely to be the initial driving force for folding the nanobelt to form the first loop for the subsequent growth. This is the nucleation of the nanoring.

As the growth continues, the nanobelt may be naturally attracted onto the rim of the nanoring due to electrostatic interaction and extends parallel to the rim of the nanoring to neutralize the local polar charge and reduce the surface area; this results in the formation of a self-coiled, coaxial, uni-radius, multilooped nanoring structure (figure 13(c)). The self-assembly is spontaneous, which means that the self-coiling along the rim proceeds as the nanobelt grows. The reduced surface area and the formation of chemical bonds (short range

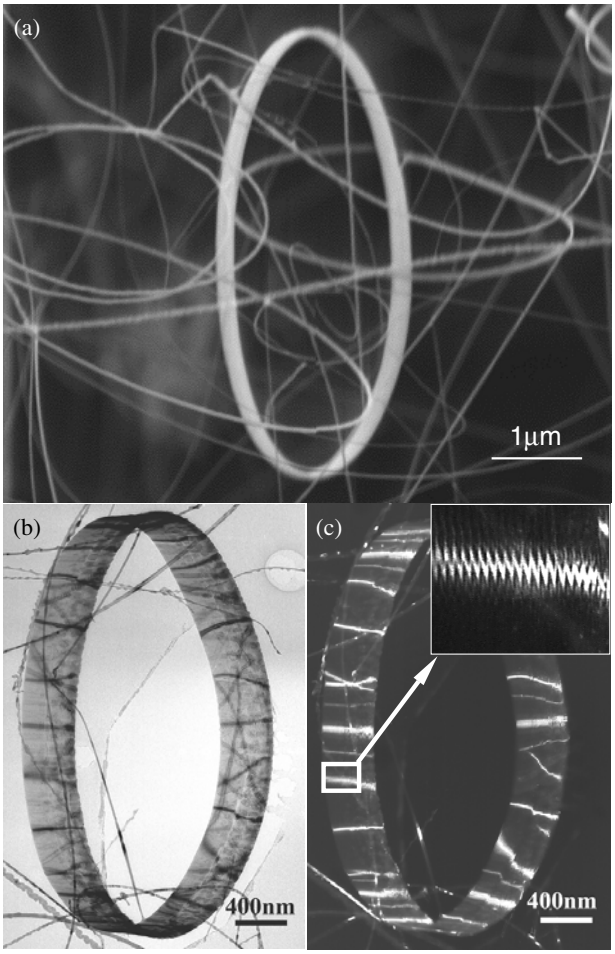

Figure 12. (a) Seamless single-crystal nanorings of ZnO. (b) Bright-field and (c) dark-field TEM images of a nanoring. The inset in (c) is an enlargement of a local region, displaying the contrast produced by the uni-radius, loop-by-loop, self-coiling nanobelt [27].

force) between the loops stabilize the coiled structure. The width of the nanoring increases as more loops wind along the nanoring axis and all of them remain in the same crystal orientation (figure 13(d)). Since the growth was carried out in a temperature region of 200–400 °C, 'epitaxial sintering' of the adjacent loops forms a single-crystal cylindrical nanoring structure and the loops of the nanobelt are joined by chemical bonds as a single entity. A uni-radius and perfectly aligned coiling is energetically favourable because of the complete neutralization of the local polar charges inside the nanoring and the reduced surface area. This is the 'Slinky' growth model of the nanoring [27]. The charge model of the nanoring is analogous to that of a single RNA helix.

6. Kinetics in nanostructure formation

6.1. Core–shell nanobelts and nanotubes

Control over growth kinetics is important in determining the nanostructures obtained. This is a complex but poorly understood area. In this section, we use Zn–ZnO core–shell structure as

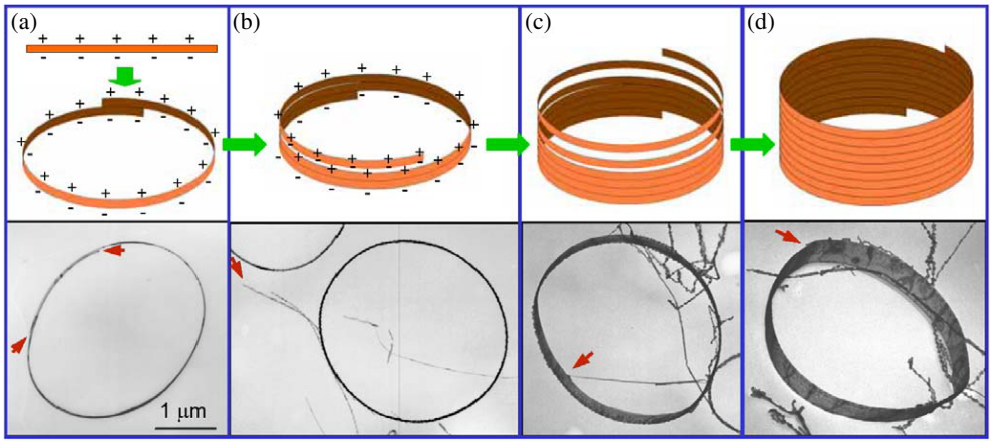

Figure 13. (a) The structure model of ZnO, showing the ± (0001) polar surfaces. ((b)–(e)) Proposed growth process and corresponding experimental results showing the initiation and formation of the single-crystal nanoring via self-coiling of a polar nanobelt. The nanoring is initiated by folding a nanobelt into a loop with overlapped ends due to long range electrostatic interaction among the polar charges; the short range chemical bonding stabilizes the coiled ring structure; and the spontaneous self-coiling of the nanobelt is driven by minimizing the energy contributed by the polar charges, surface area and elastic deformation. (f) SEM images of the as-synthesized single-crystal ZnO nanoring. (g) The 'Slinky' growth model of the nanoring. (h) The charge model of a single DNA helix, analogous to the charge model of the nanobelt during the self-coiling process [27].

an example to show the critical role played by growth kinetics in nanostructure formation [28]. In this growth process, pure ZnO powders were selected as source material, which was loaded in an alumina boat and positioned at the centre of a horizontal tube furnace. The synthesis process has two steps. The first step is controlling the evaporation and decomposition process: this was carried out by evacuating the alumina tube to $\sim 2 \times 10^{-3}$ Torr, raising the temperature to 1350 °C and holding it there for 5 min, with no carrier gas introduced. The second step is controlling the growth: this was also carried out at 1350 °C for 30 min but with an Ar carrier gas at a pressure of 200–250 Torr and flow rate of 25 sccm.

The sample was deposited on a silicon substrate, as shown by an optical image displayed in figure 14(a). The most interesting phenomenon is that the as-grown products are distributed in two distinct temperature regions, with the metallic lustre in black indicating the Zn nanobelts and the white the ZnO nanobelts. Scanning electron microscopy (SEM) images show curly Zn nanobelts (figure 14(b)) and straight ZnO nanobelts (figure 14(c)). The Zn nanobelts were formed in a temperature range of 200–300 °C and they are distributed across a region of >4 cm in length. The ZnO nanobelts were formed in a temperature range of 300–400 °C. The transition distance between the two different products is ∼0.5 cm. This apparently shows the structural control by growth temperature and kinetics. The structure of the ZnO nanobelts has been investigated previously [17]. The x-ray diffraction spectrum recorded from the metallic region indicates that the as-received product is dominated by zinc (figure 14(d)).

The epitaxial Zn–ZnO nanobelt has been analysed by high resolution TEM. Figure 15(a) is a low magnification TEM image of the nanobelt, displaying a Zn–ZnO core–shell structure. The most important point is that the shell has an epitaxial relationship with the core, as presented in the electron diffraction pattern, in which there are many weak reflection spots that were produced by double diffraction from the core and the shell. From the image and the diffraction pattern, it is apparent that the core is a single crystal and the shell is single crystalline; they have an epitaxial relationship with identical orientations. The diffraction pattern given in

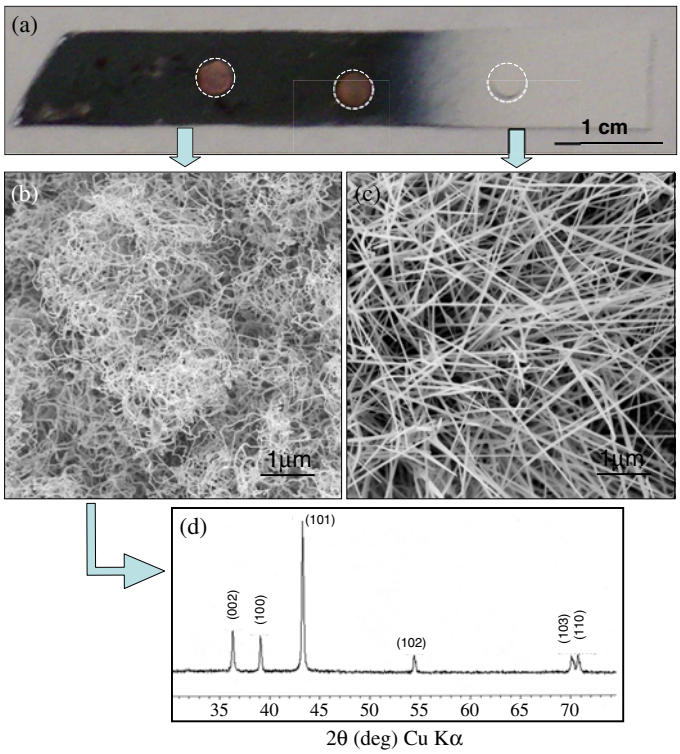

Figure 14. (a) An optical micrograph of the as-synthesized sample on a silicon substrate, showing two distinct products on the surface. The three circles indicate three TEM copper grids placed on the substrate for collecting samples. ((b), (c)) SEM images recorded from the metallic lustre and white colour regions, presenting the formation of pure Zn nanobelts and ZnO nanobelts, respectively. (d) XRD recorded from the metallic region, showing the formation of Zn nanobelts [28].

figure 15 is contributed by both Zn and ZnO but with a strong double-diffraction effect, which is responsible for producing the extra reflection spots. Structurally, Zn and ZnO both have the hexagonal crystal structure with lattice constants of $a = 0.2665$, $c = 0.4947$ and $a = 0.3249$, $c = 0.5206$ nm [29], respectively; thus, the mismatch between the two at $(10\bar{1}0)$ is $\sim$21.9% (with reference to Zn). The interference between the Bragg reflections from the two crystals produces moire fringes in the image, which are apparent in the high resolution TEM image presented in figure 15(b) in the region where the Zn core and the ZnO shell overlap. In the region where there is only ZnO shell, the HRTEM image shows clear lattice structure. The boundary between the Zn core and the ZnO shell is fairly sharp. Mismatch between the Zn core and ZnO shell produces defects and stacking faults in the interfacial region, which have been analysed in detail and is reported elsewhere [30].

Our synthesis experiment used ZnO powder as the raw material, while the products produced were Zn–ZnO core–shell nanobelts and ZnO nanobelts distributed in distinct temperature regions. It is well known that the decomposition of ZnO occurs when it is subject to high enough temperature in vacuum. The thermodynamics of these processes can be presented as the follows. The solid–vapour process and the decomposition process are expressed as

$$\mathrm{ZnO(s)} \leftrightarrow \mathrm{ZnO(g)}, \tag{1}$$

$$\mathrm{ZnO(g)} \leftrightarrow \mathrm{Zn(g)} + \tfrac{1}{2}\mathrm{O_2(g)}. \tag{2}$$

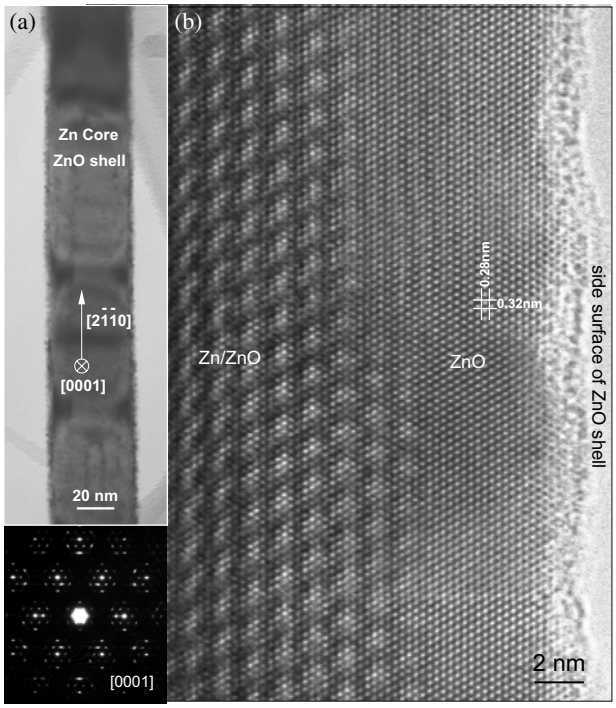

Figure 15. (a) A low magnification TEM image of a Zn–ZnO core–shell heteronanobelt. (b) A [0001] high resolution TEM image recorded near the right-hand edge of a nanobelt, showing the Zn–ZnO overlap region and the ZnO wall. The corresponding electron diffraction pattern is given below (a) (image courtesy of Dr Y Ding) [28].

The equilibrium constant function K_P for processes (1) and (2) as a function of temperature is given by

$$-R \ln K_P(T) = \Delta H^0_{298}/T + \Delta G(T), \tag{3}$$

where ΔH is the change in free energy and $\Delta G(T)$ the Gibbs energy and $K_P = (P_{\mathrm{Zn(g)}} P^{1/2}_{\mathrm{O_2}})/P^{3/2}_e$, where P_{Zn} and P_{O} are the partial pressures of Zn and O_2, respectively, and P_e is the pressure in the growth chamber. Substituting the thermodynamic data into (3), one obtains

$$\ln(P_{\mathrm{Zn(g)}} P^{1/2}_{\mathrm{O_2}}/P^{3/2}_e) = -4.855 - 2474/T. \tag{4}$$

From equation (4), the saturation vapour pressure for Zn at 1350 °C is estimated to be $\sim 10 - 3$ Torr, close to the pre-evacuated pressure in the growth chamber; hence, it is possible that part of the ZnO vapour decomposes into Zn vapour and O_2. Then, the ZnO vapour together with the Zn vapour is transported by Ar carrier gas to a lower temperature region of 200–400 °C (figure 16(a)), which is cold enough to condense the vapour phase onto the substrate. The ZnO vapour condenses in the region of 300–400 °C due to its higher sublimation temperature, resulting in the growth of ZnO nanobelts; the Zn vapour condenses in the 200–300 °C region owing to the lower sublimation temperature, resulting in the growth of Zn nanobelts, as shown in figure 16(b). The Zn nanobelts are dominated by the large (0001) facet due to it having the lowest surface energy.

On the other hand, the residual oxygen in the growth chamber as well as the oxygen decomposed originally from the raw material can oxidize the surface of the Zn nanobelts,

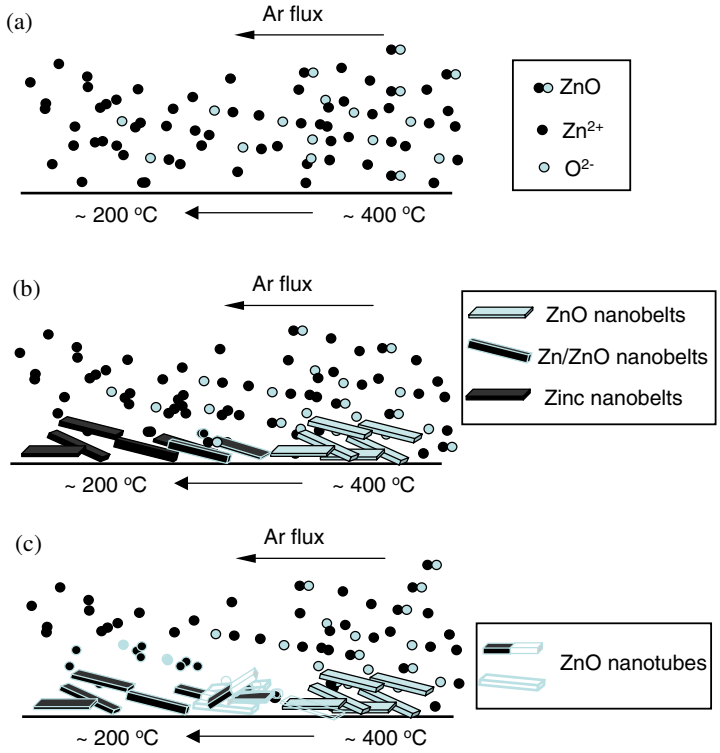

Figure 16. A proposed growth mechanism for the formation of the Zn–ZnO core–shell nanobelts and ZnO nanotubes. (a) ZnO, Zn and O_2 vapour phases decomposed from pure ZnO raw materials at high temperature and carried by the Ar gas. (b) Deposition of the vapours in different substrate temperature regions results in the formation of ZnO nanobelts and Zn nanobelts, which subsequently transform into Zn–ZnO core–shell heteronanobelts after surface oxidation. (c) Vaporization/sublimation of the Zn core results in the formation of ZnO nanotubes.

resulting in the formation of a thin ZnO shell on the surface. Since both Zn and ZnO have the hexagonal crystal structure, the ZnO shell tends to have an epitaxial orientation relationship with the Zn core, forming Zn–ZnO core–shell nanobelts.

Moreover, Zn has a much lower melting point, of 419 °C, than ZnO, 1975 °C; it is possible for Zn to be sublimated out of the nanobelt at temperatures of 200–300 °C, resulting in the formation of ZnO nanotubes (figure 16(c)).

6.2. Nanocages

By changing the composition of the source material, nanocages of ZnO shells have been grown [31]. A mixture of commercial ZnO, SnO_2 and graphite powders in an atomic ratio of 2:1:1 was used as the source material. Thermal evaporation was conducted at 1150 °C for 15 min under pressure of 200–300 Torr and with an Ar flow rate 25 sccm (standard cubic centimetres per minute); then the sample was cooled down to 1000 °C and kept isothermal for 30 min without supplying any Ar gas. In the temperature zone of 300–500 °C that we are interested in, balls and polyhedra are observed; some of them are dispersed on the substrate and there appears to be no correlation among them (figure 17(a)), while some of them line up along a ZnO nanobelt (figure 17(b)) that was formed in a higher temperature zone of typically 700–900 °C. Hexagon based rods are often seen (figure 17(c)) but they have shell structure.

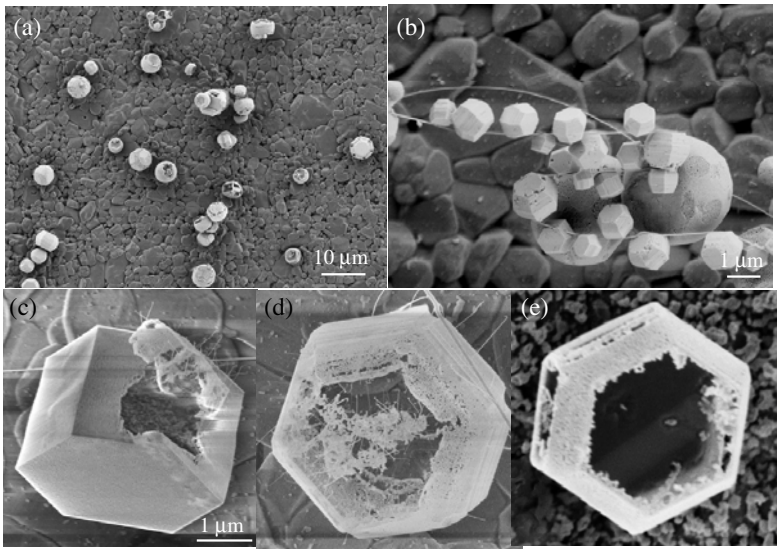

Figure 17. Low magnification SEM images of ZnO polyhedral cages and shells (a) distributed dispersively on the substrate and (b) aligned along a nanobelt, respectively. ((c)–(e)) Typical drum shaped cages of truncated hexagon based shells (image courtesy of P X Gao) [31].

The polyhedron is enclosed by (0001) (top and bottom surface), $\{10\bar{1}0\}$ (side surfaces), stepped $\{10\bar{1}1\}$ (inclined surfaces) and high index planes with rough surfaces. Some truncated hexagon based drums show open corners, such as the one displayed in figure 17(d). In some cases, one side of the shell collapses possibly due to the high growth temperature as well as the small shell thickness (figure 17(e)). A common feature is that the shell exhibits mesoporous structure. Although the polyhedral shell structure appears to be composed of nanocrystals, transmission electron diffraction and imaging indicates that they have a 'single-crystalline' textured orientation and the side surfaces are $\{10\bar{1}0\}$. These types of shell structures could be candidates for drug delivery use.

7. Doped ZnO nanobelts

Diluted magnetic semiconductors (DMS) are promising materials for spintronics (spin + electronics) use, a proposed technology that uses the electron spin rather than the electron charge for reading and writing information [32, 33]. Much of the recent effort towards spintronics has been focused on the synthesis and characterization of manganese doped III–V and II–VI materials, with prominent interest in GaN:Mn and ZnO:Mn due to a proposed and measured Curie temperature above room temperature [34]. The integration of DMS materials into today's electronics will require very low dimensions in order to make real use of the advantages offered by spin, but the majority of the recent studies focused on bulk materials. Furthermore, for future goals, a technique for doping nanosized structures has to be established, offering precise control of the species in both concentration and lateral position.

We have used ion implantation to modify the electrical and optical properties of ZnO nanobelts, aiming at developing quasi-one-dimensional nanomaterial for spintronics [35]. Ion implantation of $^{55}Mn^{+}$ ions into ZnO nanobelts was carried out at room temperature with an ion energy of 30 keV and a flux of 1×10^{15} cm^{-2}. Figure 18 shows TEM images of the as-implanted ZnO nanobelt, displaying numerous stacking faults generated in the volume.

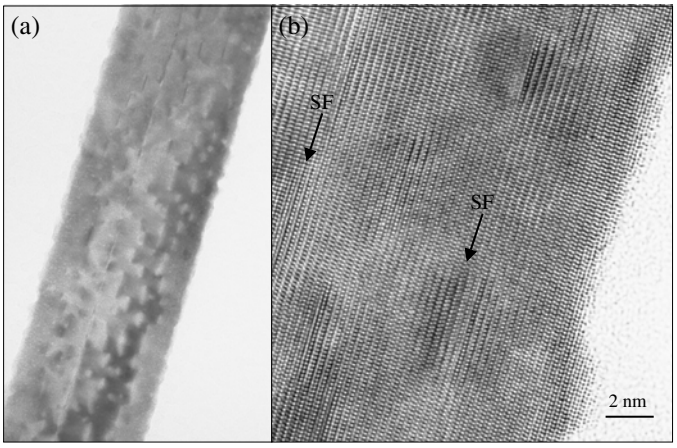

Figure 18. (a) Bright-field and dark-field TEM images of ZnO nanobelts doped with Mn. The inset is the corresponding electron diffraction pattern. (b) A high resolution TEM image of the doped nanobelt, showing numerous miniature stacking faults (SF) confined in the *c*-plane. The stacking fault terminated inside the nanobelt with the creation of partial dislocations (image courtesy of Dr C Ronning) [35].

The high resolution TEM image clearly reveals the fine details of the atomic lattice in the vicinity of the Mn ion induced stacking faults. Damage at the surface of the nanobelt is also visible. We have found that annealing the sample at different temperature can control the density of stacking faults, possibly resulting in tunable electrical and optical properties.

8. Properties, potential applications and novel devices

8.1. Luminescent property

ZnO exhibits a direct band-gap of 3.37 eV at room temperature with a large exciton energy of 60 meV. The strong exciton binding energy, which is much larger than that of GaN (25 meV), and the thermal energy at room temperature (26 meV) can ensure an efficient exciton emission at room temperature under low excitation energy. As a consequence, ZnO is recognized as a promising photonic material in the blue–UV region.

Single-crystalline ZnO nanowires have been synthesized using high temperature VLS growth methods. Room temperature UV lasing in ZnO nanowires has been demonstrated [36]. PL spectra of the ZnO nanorods were measured with a fluorescence spectrophotometer using a Xe lamp with an excitation wavelength of 325 nm at room temperature. Figure 19 shows the PL spectrum of the ZnO nanorods with a diameter in the range 60 ± 80 nm. Three emitting bands, including a strong ultraviolet emission at around 386 nm and a very weak blue band (440 ± 480 nm) as well as an almost negligible green band (510 ± 580 nm), were observed. The UV emission must be contributing to the near band edge emission of the wide band-gap ZnO. It has been suggested that the green band emission corresponds to the singly ionized oxygen vacancy in ZnO and results from the recombination of a photogenerated hole with the singly ionized charge state of this defect. The stronger the intensity of the green luminescence, the more singly ionized oxygen vacancies there are. Thus the almost negligible green band in figure 19 shows that there is a very low concentration of oxygen vacancies in the well-aligned ZnO nanorods. The observation of blue band emission (440 ± 480 nm) of ZnO film has also been reported, using cathodoluminescence.

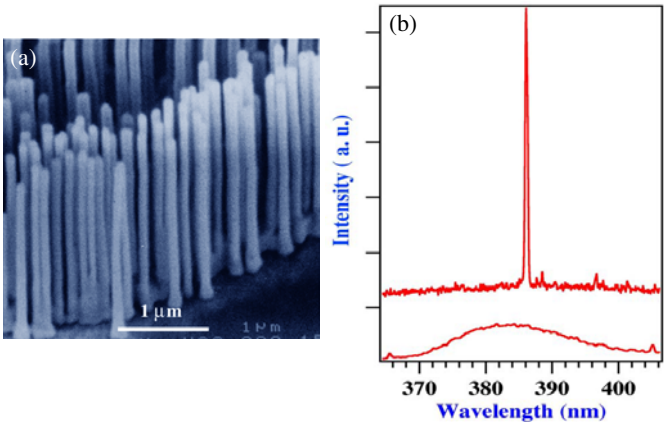

Figure 19. (a) An SEM image of aligned ZnO nanowire arrays grown on sapphire substrate coated with a 3 nm thick layer of Au. (b) Emission spectra from nanowire arrays at pump powers of 20 and 100 kW cm^{-2}. The spectra are offset for easy comparison. Stimulated emission from the nanowires was collected in the direction along the nanowire's end-plane normal (the symmetric axis) with a monochromator. All experiments were carried out at room temperature (courtesy of Dr Peidong Yang) [36].

8.2. Field effect transistor

Field effect transistors have been fabricated using individual nanobelts [37]. Large bundles of either SnO_2 or ZnO nanobelts were dispersed in ethanol by ultrasonication until mostly individual nanobelts were isolated. These ethanol dispersions were dried onto a SiO_2/Si substrate for imaging by non-contact mode atomic force microscopy (AFM). SnO_2 field effect transistors were fabricated by depositing SnO_2 nanobelt dispersions onto $SiO_2/Si(p^+)$ substrates; this was followed by treatment in an oxygen atmosphere at 800 °C for 2 h. The SiO_2/Si substrates were then spin coated with PMMA, baked, exposed to electron-beam lithography for the definition of electrode arrays and developed. A 30 nm thick layer of titanium was deposited by electron-beam evaporation to serve as the source and drain electrodes and the remaining PMMA was lifted off in hot acetone. An AFM image of the field effect transistor (FET) and a schematic diagram are shown in figure 20. The principle of this device is that controlling the gate voltage would control the current flowing from the source to the drain.

An alternative way of contacting the nanostructures was applied to ZnO nanobelts. In this case, field effect transistors were fabricated by depositing dispersed ZnO nanobelts on predefined gold electrode arrays. In both cases, the SiO_2 gate dielectric thickness was 120 nm and the back gate electrode was fabricated by evaporation of gold on the $Si(p^+)$ side of the substrate. Also, in both fabrication schemes, the electrode arrays were variably spaced. They included electrode gaps as small as 100 nm and as large as 6 μm.

By forming metal electrode/nanostructure electrical contacts and capacitively coupling the nanostructure to a nearby gate electrode, an FET is produced using a nanobelt that allows the exploration of new aspects of the physical and chemical properties of the nanostructures [38–40].

The alternative way of contacting the nanobelts by simply depositing them on top of pre-fabricated gold electrodes led to very resistive contacts. A typical ZnO field effect transistor showed a gate threshold voltage of -15 V, a switching ratio of nearly 100 and a peak conductivity of $1.25 \times 10^{-3}\ \Omega^{-1}\ cm^{-1}$. A completely analogous behaviour has been observed in the case of carbon nanotubes deposited on top of Au electrodes or covered by Ti electrodes [41].

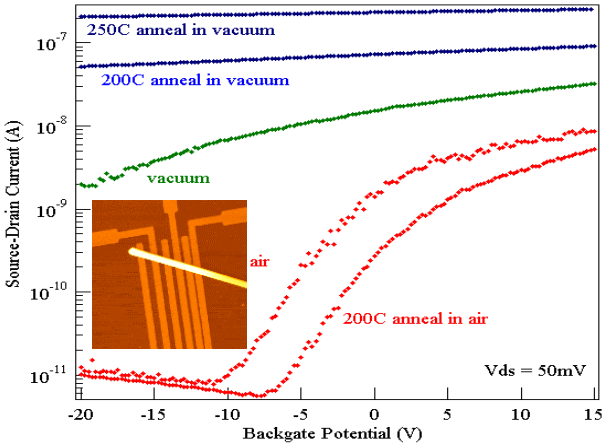

Figure 20. SnO_2 nanobelt FET oxygen sensitivity. Source–drain current versus gate bias for a SnO_2 FET after various treatments measured in this order: air, vacuum, 200 °C vacuum anneal, 250 °C vacuum anneal, 200 °C air anneal. The inset shows a field effect transistor (FET) device made using a single nanobelt (courtesy of M Arnold and Dr P Avouris) [37].

8.3. Tunable electrical properties

The conductivity of a nanobelt can be tuned by controlling its surface and volume oxygen deficiency [37]. Before electrical measurement, SnO_2 nanobelts are annealed in 1 atm oxygen environment at 800 °C for 2 h. Without this treatment, the as-produced nanobelts exhibit no measurable conductivity for source–drain biases from −10 to 10 V and for gate biases from −20 to 20 V, while after this treatment the SnO_2 nanobelts exhibit considerable conductivity. By further annealing of the devices at lower temperatures in vacuum, oxygen or *ambient* the electrical properties of the nanobelts can be tuned.

After annealing the SnO_2 devices in vacuum at 200 °C, the nanobelt conductivity is observed to increase along with an associated negative shift in gate threshold voltage. Smaller, additional increases in conductivity are observed after additional vacuum anneals. Eventually, the nanobelt behaves like a metal with the gate field being unable to affect the current flowing through the device. In contrast, annealing nanobelt devices in *ambient* at 200 °C leads to a decrease of the conductivity, along with a shift in the gate threshold voltage in the opposite, positive direction (figure 20). The source–drain conductivity at zero gate bias spans three orders of magnitude from 0.09 Ω^{-1} cm^{-1} after annealing at 200 °C in *ambient* to 75.3 $\Omega^{-1}cm^{-1}$ after annealing at 250 °C in vacuum. The changes in conductivity with low temperature annealing most likely result from variations in the number of oxygen species adsorbed on the SnO_2 surfaces or in the number of oxygen vacancies in the SnO_2 bulk with the amount of oxygen in the environment [42]. The number of equilibrium surface and bulk oxygen defects will be a function of the environmental oxygen partial pressure and temperature. Annealing in vacuum should decrease the number of adsorbed oxygen species and increase the number of bulk oxygen vacancies, while annealing in oxygen or *ambient* should do the opposite. It is well established that bulk and surface oxygen vacancies in SnO_2 act as electron donors, which should increase SnO_2 conductivity and decrease the gate threshold voltage [43]. This is precisely what we observe.

It should be noted that the SnO_2 nanobelt conductivity is observed to increase and the gate threshold voltage is observed to decrease simply on taking a nanobelt device from ambient

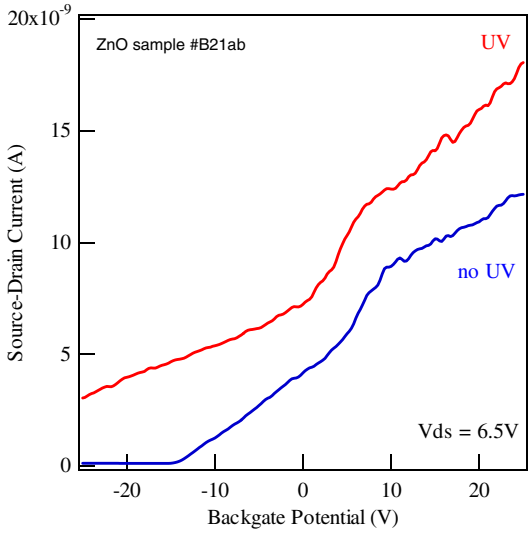

Figure 21. The source–drain current measured from a ZnO nanobelt FET, showing a strong dependence on the UV illumination (courtesy of M Arnold and Dr P Avouris) [37].

into vacuum without annealing (figure 20). Since the diffusion of bulk oxygen vacancies at room temperature will be limited [44, 45], this indicates that surface oxygen desorption is most likely taking place at this temperature. Because of their small dimensions, semiconducting oxide nanobelts will have of the order of 10^{20} surface oxygen sites per cubic centimetre of material [46]. Thus, even for partial changes in the concentration of adsorbed oxygen species, large changes in nanobelt conductivity can be observed.

The strong dependence of the conductance on the oxygen deficiency in nanobelts is an important characteristic of functional oxide, using which one can tune and control the electrical properties of the nanodevice.

8.4. Photoconductivity

Ultraviolet light irradiation of the nanobelt diode of SnO_2 in air is observed to result in a significant increase of the conductivity (figure 21). Light with a wavelength of 350 nm ($E_\lambda = 3.54$ eV) was used, exceeding the direct band-gap of SnO_2. The increase in the conductivity results from both photogeneration of electron–hole pairs as well as doping by UV light induced surface desorption [47–49]. These processes could be observed by introducing a shutter between the light source and the SnO_2 nanobelt so that the flux of UV photons could be turned on and off.

The unique geometrical shape of nanobelts is ideal for field emission. MoO_3 nanobelts have been shown to exhibit superior performance. The work function at the tips of individual ZnO nanobelts has been measured by a novel technique [50].

8.5. Gas, chemical and biosensors

Conductometric metal oxide semiconductor thin films are the most promising devices among solid state chemical sensors, due to their small dimension, low cost, low power consumption, on-line operation and high compatibility with microelectronic processing. The fundamental sensing mechanism of metal oxide based gas sensors relies on a change in electrical

conductivity due to the process of interaction between the surface complexes such as O^-, O_2^-, H^+ and OH^- reactive chemical species and the gas molecules to be detected.

Although a large number of different oxides have been investigated for their gas sensing properties, commercially available gas sensors are mainly made of SnO_2 in the form of thick films, porous pellets or thin films. The effects of the microstructure, i.e., the ratio of the surface area to volume, grain size and pore size of the metal oxide particles, as well as the film thickness of the sensor, are well recognized. Lack of long term stability has until today prevented a wide ranging application of such sensors. Nanobelts of semiconducting oxide, with a rectangular cross section in a ribbon-like morphology, are very promising for sensor use due to the fact that the surface to volume ratio is very high, the oxide is single crystalline, the faces exposed to the gaseous environment are always the same and the size is likely to produce a complete depletion of carriers inside the belt [51]. Also, the deposition technique is very simple and cheap, and the size and shape can be easily controlled. In the polycrystalline and thick film devices, only a small fraction of the adsorbed species adsorbed near the grain boundaries is active in modifying the device electrical transport properties. In the new sensors based on single-crystalline nanobelts, almost all of the adsorbed species are active in producing a surface depletion layer. Free carriers should cross the belts bulk along the axis in a FET channel-like way. Besides this, since the depletion layer for tin oxide, due to oxygen desorption, penetrates 50 nm or more through the bulk, the belts are probably almost as depleted of carriers as a pinched-off FET because the belt thickness is typically less than 50 nm. The presence of poisoning species should switch the structures from the pinched-off to the conductive channel, strongly modifying the electrical properties. With a further reduction of belt size we could envisage the development of quantum confined structures and nanodevices.

For the fabrication of sensors, a platinum interdigitative electrode structure was made using lithography and a metal deposition technique on an alumina substrate. A platinum heater was attached to the back of the substrate in order to control the working temperature of the sensor. Then, a bunch of nanobelts was placed onto the electrodes for measuring their electric conductance and an appropriate measurement was taken to ensure the contact of the nanobelts with the electrodes. The flow-through technique is used to determine the gas sensing properties of the thin films. A constant flux of synthetic air equal to 0.3 l min^{-1}, mixed with the desired amount of gaseous species, flows through a stabilized sealed chamber at 20 °C, at atmospheric pressure and with controlled humidity. Electrical characterization was carried out by a volt–amperometric technique at a constant bias of 1 V and a picoammeter measured the change of electrical current.

Figure 22 reports the isothermal response of the current flowing through the tin oxide nanobelts as two square concentration pulses of CO (250 and 500 ppm respectively) are fed into the test chamber, at a working temperature of 400 °C and 30% RH (relative humidity at 20 °C). The electric current increases by about 60% and 100% with the introduction of 200 and 500 ppm CO. The sensor response, defined as the relative variation in conductance due to the introduction of gas, is about $\Delta G/G = 0.9$.

Figure 22 also shows the isothermal response of the current flowing through the nanobelts as a square concentration pulse of 0.5 ppm nitrogen dioxide is fed into the test chamber, at a working temperature of 400 °C and 30% RH. The sensor response is $\Delta G/G = -15.5 = -1550\%$, which is extremely high and sensitive. This means that the sensitivity of the sensor is at the level of a few ppb.

In general, the selectivity of the oxide is a concern. This may be improved by fabricating sensors using several different types of nanobelts, or by functionalizing the surfaces of the nanobelts. It is, however, very important to note that the CO and ethanol increase the conductivity, while NO_2 decreases the conductivity of the SnO_2 nanobelts.

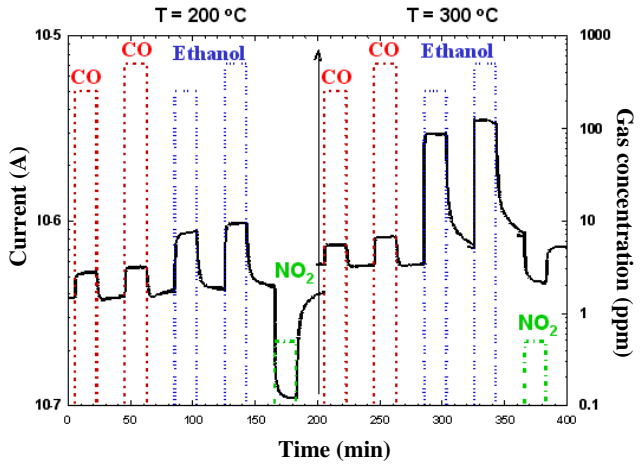

Figure 22. Gas sensors made using nanobelts. The response of the conductance through SnO_2 nanobelts to the concentration of the surface adsorbed CO, ethanol and NO_2 gases at two different temperatures (courtesy of Dr E Comini) [51].

The small size offered by the sensors based on individual nanobelts is a major advantage for application in biotechnology, because it gives the potential for implantation in biological systems. Nanosensors based on nanobelts may be unique in detecting single cancer cells and measuring pressure in biofluid.

8.6. Thermal conductivity

Heat transport at the nanoscale is a very interesting and technologically important area. With the reduction of object size, phonon modes and phonon densities of states change drastically, resulting in unusual thermal transport phenomena in mesoscopic systems. Theoretical investigation of thermal conductance in a one-dimensional nanowire predicted a quantum effect at very low temperature: $G_{\mathrm{th}} = \pi^2 k_{\mathrm{B}}^2 T/3$ h [52]. Experimental measurement has proved the prediction [53]. Thermal transport along a single SnO_2 nanobelt has also been carried out (figure 23(a)) [54]. Thermal contact micropads have been fabricated using a lithography technique. The thermal conductance across the nanobelt measured as a function of the local temperature is given in figure 23(b). The thermal conductivity of the nanobelts is significantly suppressed in comparison to that in the bulk due to increased phonon–boundary scattering and modified phonon dispersion [55]. This size effect can lead to localized heating in nanoelectronics [56], but may find potential use in improving thermoelectric performance.

8.7. Nanobelts as nanoresonators

Another key quantity in the application of the nanobelt is its bending modulus. We have measured this quantity using a technique developed for carbon nanotubes. On the basis of the electric field induced resonant excitation, the mechanical properties of individual nanowire-like structures can be measured by *in situ* transmission electron microscopy (TEM) [57, 58]. Using this method, mechanical properties of carbon nanotubes [59], silicon nanowires [60] and silicon carbide–silica composite nanowires [60] have been obtained.

To carry out the mechanical property measurements on a nanobelt, a specimen holder for a Hitachi HF-2000 TEM (200 kV) was built to apply a voltage across the nanobelt and its counter-electrode. Mechanical resonance can be induced if the applied frequency matches the

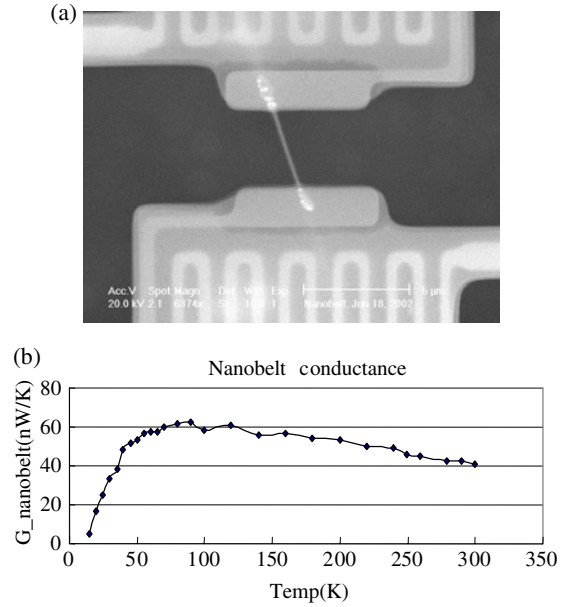

Figure 23. Measurement of thermal transport through a single SnO_2 nanobelt (image courtesy of Dr L Shi) [54].

natural resonance frequency of the nanobelt. Due to the mirror symmetry of the nanobelt, there are two distinct fundamental resonance frequencies corresponding to the vibration in the thickness and width directions, which are given from classical elasticity theory: as [61]

$$\nu_x = \frac{\beta_1^2 T}{4\pi L^2}\sqrt{\frac{E_x}{3\rho}}, \tag{5}$$

$$\nu_y = \frac{\beta_1^2 W}{4\pi L^2}\sqrt{\frac{E_y}{3\rho}}, \tag{6}$$

where $\beta_1 = 1.875$ for the first-harmonic resonance; E_x and E_y are the bending moduli if the vibration is along the x-axis (thickness direction) and y direction (width direction), respectively; ρ is the density, L is the length, W is the width and T is the thickness of the nanobelt. The two modes are decoupled and they can be observed separately in experiments.

Changing the frequency of the applied voltage, we found two fundamental frequencies in two orthogonal directions transverse to the nanobelt [62]. Figures 24(a) and (b) show the harmonic resonance with the vibration planes nearly perpendicular and parallel to the viewing direction, respectively. For calculating the bending modulus, it is critical to accurately measure the fundamental resonance frequency (ν_1) and the dimensional sizes (L and T or W) of the ZnO nanobelts investigated. To determine ν_1, we have checked the stability of the resonance frequency to ensure that one end of the nanobelt is tightly fixed and the resonant excitations have been carefully checked around the half-value of the resonance frequency. The specimen holder can be rotated about its axis so that the nanobelt can be aligned perpendicular to the electron beam, so the real length (L) of the nanobelt can be measured. The projection direction along the beam is determined from the electron diffraction pattern, so the true thickness and width can be determined because the normal direction of the nanobelt is $[2\bar{1}\bar{1}0]$. On the basis of on the experimental data, the bending moduli of the ZnO nanobelts can be calculated

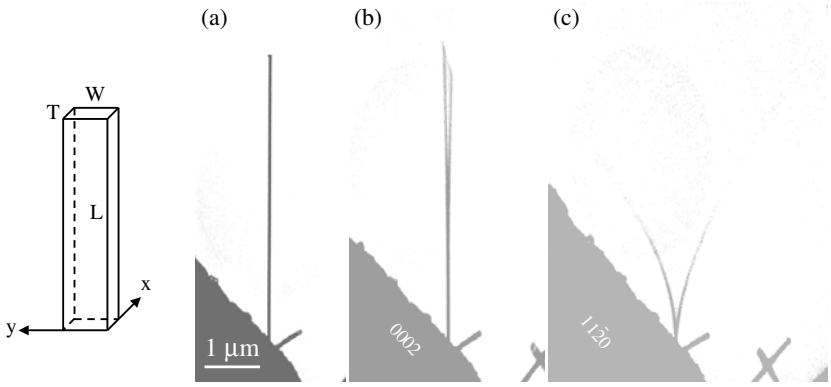

Figure 24. Nanoresonators made of nanobelts. Measuring the bending modulus of a ZnO nanobelt by means of electric field induced mechanical resonance in TEM. (a) The geometrical shape of a nanobelt; ((b), (c)) mechanical resonance of a nanobelt along the two orthogonal directions, respectively closely perpendicular to the viewing direction ($\nu_x = 622$ kHz) and nearly parallel to the viewing direction ($\nu_y = 691$ kHz) (courtesy of Dr X D Bai) [50].

using equations (1) and (2). The bending modulus of the ZnO nanobelts was ∼52 GPa. Our experiment clearly shows that nanobelts can be effective nanoresonators exhibiting two orthogonal resonance modes, which can be used as probes for SPM operated in tapping and scanning modes.

Using a technique developed for measuring the work function at the tip of a carbon nanotube [63], the work function at the tip of an oxide nanobelt has also been measured [64].

8.8. Nanocantilevers

The cantilever based scanning probe microscopy (SPM) technique is one of the most powerful approaches in imaging, manipulating and measuring nanoscale properties and phenomena. The most conventional cantilever used for SPM is based on silicon, Si_3N_4 or SiC, which is fabricated by an e-beam or optical lithography technique and has, typically, dimensions of thickness ∼100 nm, width ∼5 μm and length ∼50 μm. Utilization of nanowire and nanotube based cantilevers can have several advantages for SPM. Carbon nanotubes can be grown on the tip of a conventional cantilever and used for imaging surfaces with a large degree of abrupt variation in the surface morphology [65]. We have demonstrated the manipulation of nanobelts by AFM and its potential for use in nanocantilevers [66].

Combining microelectromechanical system (MEMS) technology with self-assembled nanobelts we are able to produce cost effective cantilevers with much heightened sensitivity for a range of devices and applications. Force, pressure, mass, thermal, biological and chemical sensors are all prospective devices. Semiconducting nanobelts are ideal candidates for cantilever applications. Structurally they are defect free single crystals, providing excellent mechanical properties. The reduced dimensions of nanobelt cantilevers offer a significant increase in cantilever sensitivity. Combining the aforementioned techniques with micromanipulation has led to the horizontal alignment of individual ZnO nanobelts onto silicon chips. The aligned ZnO cantilevers, shown in figure 25 below, were manipulated to have a range of lengths. This exemplifies our ability to tune the resonance frequency of each cantilever and thus modify cantilevers for different applications such as contact, non-contact and tapping mode AFM. Periodic contrast of the ZnO cantilevers is observed as a result of electronic charge induced vibrations during SEM operation. Such contrast is absent in regions where the

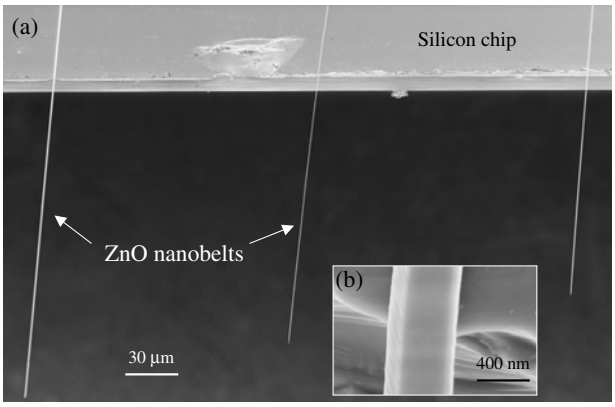

Figure 25. (a) Nanobelts as ultrasmall nanocantilever arrays aligned on a silicon chip. (b) An enlarged SEM image recorded from the nanobelt cantilever (courtesy of W Hughes) [66].

nanobelts are in direct contact with the silicon substrate, suggesting adequate adhesion forces between the cantilevers and the silicon chip.

8.9. Piezoelectricity of the polar nanobelts

Piezoelectricity is due to atomic scale polarization. To illustrate the piezoelectricity, one considers an atom with a positive charge that is surrounded tetrahedrally by anions (figure 26(a)). The centre of gravity of the negative charges is at the centre of the tetrahedron. On exerting a pressure on the crystal along the cornering direction of the tetrahedron, the tetrahedron will experience a distortion and the centre of gravity of the negative charges will no longer coincide with the position of the positive central atom; an electric dipole is generated. If all of the tetrahedra in the crystal have the same orientation or some other mutual orientation that does not allow for a cancellation among the dipoles, the crystal will have a macroscopic dipole. The two opposite faces of the crystal have opposite electric charges.

'Piezoelectricity' refers to a reverse process in which a contraction or elongation is created in the crystal once it is positioned in an electric field. Crystals can only be piezoelectric if they are non-centrally symmetric, ensuring non-compensation among the dipoles created by the tetrahedra. The piezoelectric effect can convert a mechanical vibration into an electric signal or vice versa. It is widely used in resonators, controlling tip movement in scanning probe microscopy, sensors for vibration waves in air and under sea etc.

Piezoelectricity is different from ferroelectricity or ferromagnetism. Ferroelectricity originates from an electric dipole moment induced by the spontaneous polarization of the crystal and ferromagnetism is based on the atomic magnetic moment induced by the electron spin. Ferroelectricity and ferromagnetism have many common characteristics, such as domains and hysteresis loops. If the dipoles can be made to cancel each other by the randomly orientation of ferroelectric domains, the material does not exhibit a macroscopic dipole. It is called paraelectric. If these dipole domains cannot cancel each other, the residual dipoles will add up, forming a macroscopic dipole, which gives ferroelectricity. Piezoelectricity, however, originates from the polarization of the tetrahedrally coordinated unit and it is a crystal structure determined effect. On the nanometre scale, ferroelectricity and ferromagnetism may be greatly reduced or vanish, but piezoelectricity is preserved with a possibility of enhanced performance due to the free boundary for volume expansion/contraction.

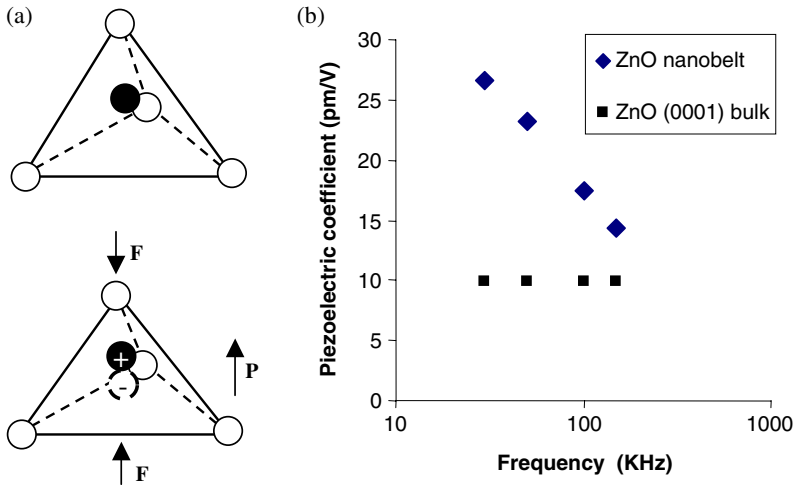

Figure 26. (a) Schematic diagrams showing the piezoelectric effect in a tetrahedrally coordinated cation–anion unit. (b) The experimentally measured piezoelectric coefficient d_{33} for ZnO and its comparison to that of the bulk (courtesy of Dr Scott Mao and Minhua Zhao) [67].

The piezoelectric coefficient of a ZnO nanobelt has been measured by atomic force microscopy using a conductive tip [67]. After coating a (100) Si wafer with 100 nm Pd, ZnO nanobelts were dispersed on the conductive surface. Then the whole surface was coated with another 5 nm Pd coating, which served as an electrode on the ZnO nanobelt for getting a uniform electric field and avoiding electrostatic effects. Extra care was taken to ensure that the top and bottom surfaces of the nanobelt was not short-circuited after Pd deposition. The ZnO nanobelt was located by a commercially available AFM in the tapping mode. Piezoresponse force microscopy (PFM) is used to measure the effective piezoelectric coefficient (d_{33}) of individual (0001) surface dominated zinc oxide nanobelts lying on a conductive surface. On the basis of references of bulk (0001) ZnO and x-cut quartz, the effective piezoelectric coefficient d_{33} of ZnO nanobelt is found to be frequency dependent and varies from 14.3 to 26.7 pm V^{-1} (figure 26(b)), which is much larger than the value for bulk (0001) ZnO, of 9.93 pm V^{-1}. The results suggest applications of ZnO nanobelts as nanosensors and nanoactuators.

9. Outlook

This article reviews novel ZnO nanostructures grown by a solid–vapour phase technique. The various growth morphologies are summarized and their growth processes are proposed. ZnO is a semiconducting, piezoelectric and pyroelectric material. Utilizing individual nanobelts, devices and applications have been demonstrated for field effect transistors, gas sensors, nanoresonators and nanocantilevers. These derives will have important applications in nanosystems and biotechnology.

The nanobelts and relevant nanostructures are a unique group that is likely to have important applications in nanosize electronic, optical, sensor and optoelectronic devices. As for the future nanotechnology and applications in nanosystems and biotechnology, there are a lot of issues that we have to investigate:

(1) Controlled growth is required to control their size, size distribution, shape, crystal structure, defect distribution and even surface structure (atomic termination, surface

polarization). A thorough understanding of the growth mechanism(s) is the key. In processing, a valid way to control the size of the nanobelts is to properly control the temperature, pressure and growth time.

(2) Techniques are required to grow the nanobelts into aligned arrays, onto patterned substrates, in self-assembly structures with functionality. This is a key step toward nanosystem integration.

(3) For sensor applications, the nanobelts may have the required sensitivity, but the selectivity needs to be improved. This requires the synthesis of composite nanobelts, such as heterostructures, junctions and barriers. Exploration of complex oxides involving two or more types of cations is needed to improve their multifunctionality. Surface functionalization of the nanobelts is also an important direction.

(4) Finally, development of techniques for integration of nanobelts with other nanostructures and microstructures, such as nanoelectromechanical systems (NEMS) and biosensing systems, is required.

Acknowledgments

The results reviewed in this paper were partially contributed from our group members and collaborators: Xiang Yang Kong, Puxian Gao, Yong Ding, Xuedong Bai, Rusen Yang, Carsten Ronning, Zhengwei Pan, William Hughes, Daniel Moore, Chris Ma, Xudong Wang, Yolande Berta, Li Shi, M S Arnold, Ph Avouris, E Comini, G Faglia, G Sberveglieri, Enge Wang, Minhua Zhao and Scott X Mao, to whom we are very grateful. This research was supported by NSF, NASA and DARPA.

References

[1] Dulub O, Boatner L A and Diebold U 2002 *Surf. Sci.* **519** 201
[2] Meyer B and Marx D 2003 *Phys. Rev.* B **67** 035403
[3] Tasker P W 1979 *J. Phys. C: Solid State Phys.* **12** 4977
[4] Dulub O, Diebold U and Kresse G 2003 *Phys. Rev. Lett.* **90** 016102
[5] Wander A, Schedin F, Steadman P, Norris A, McGrath R, Turner T S, Thornton G and Harrison N M 2001 *Phys. Rev. Lett.* **86** 3811
[6] Staemmler V, Fink K, Meyer B, Marx D, Kunat M, Gil Girol S, Burghaus U and Woll Ch 2003 *Phys. Rev. Lett.* **90** 106102
[7] Ding Y, Kong X Y and Wang Z L 2004 *Phys. Rev.* B submitted
[8] Dai Z R, Pan Z W and Wang Z L 2003 *Adv. Funct. Mater.* **13** 9
[9] Huang M H, Wu Y Y, Feick H, Tran N, Weber E and Yang P D 2001 *Adv. Mater.* **13** 113
[10] Wagner R S and Ellis W C 1964 *Appl. Phys. Lett.* **4** 89
[11] Westwater J, Gosain D P, Tomiya S, Usui S and Ruda H 1997 *J. Vac. Sci. Technol.* B **15** 554
[12] Morales A M and Lieber C M 1998 *Science* **279** 208
[13] Gao P X and Wang Z L 2002 *J. Phys. Chem.* B **106** 12653
[14] Gao P X and Wang Z L 2003 *Nano Lett.* **3** 1315
[15] Gao P X and Wang Z L 2002 *J. Phys. Chem.* B **106** 12653 + cover
[16] Lao J Y, Huang J Y, Wang D Z and Ren Z F 2003 *Nano Lett.* **3** 235
[17] Pan Z W, Dai Z R and Wang Z L 2001 *Science* **291** 1947
[18] Wang X D, Ding Y, Summers C J and Wang Z L 2004 *J. Phys. Chem.* B at press
[19] Zhong J, Muthukumar S, Chen Y, Lu Y, Ng H M, Jiang W and Garfunkel E L 2003 *Appl. Phys. Lett.* **83** 3401
[20] Hashimoto S and Yamaguchi A 1996 *J. Am. Ceram. Soc.* **79** 1121
[21] Vigue F, Vennegues P, Vezian S, Laugt M and Faurie J P 2001 *Appl. Phys. Lett.* **79** 194
[22] Wang Z L, Kong X Y and Zuo J M 2003 *Phys. Rev. Lett.* **91** 185502 + cover
[23] Moore D, Ronning C, Ma C and Wang Z L 2004 *Chem. Phys. Lett.* **385** 8
[24] Ma C, Ding Y, Moore D, Wang X D and Wang Z L 2004 *J. Am. Chem. Soc.* **126** 708
Ma C, Ding Y, Moore D, Wang X D and Wang Z L 2004 *Nature* **427** 497 (Feature)

[25] Kong X Y and Wang Z L 2003 *Nano Lett.* **3** 1625 + cover
[26] Kong X Y and Wang Z L 2004 *Appl. Phys. Lett.* **84** 975 + cover
[27] Kong X Y, Ding Y, Yang R S and Wang Z L 2004 *Science* **303** 1348
[28] Kong X Y, Ding Y and Wang Z L 2004 *J. Phys. Chem.* B **108** 570
[29] Gallaso F 1970 *Structure and Properties of Inorganic Solids* (New York: Pergamon)
[30] Ding Y, Kong X Y and Wang Z L 2003 *J. Appl. Phys.* **95** 306
[31] Gao P X and Wang Z L 2003 *J. Am. Chem. Soc.* **125** 11299
[32] Wolf S A, Awschalom D D, Buhrmann R A, Daughton J M, von Molnar S, Roukes M L, Chtchelkanova A Y and Treger D M 2001 *Science* **294** 1488
[33] Prinz G A 1998 *Science* **282** 1660
[34] Dietl T, Ohno H, Matsukura F, Cibert J and Ferrand D 2000 *Science* **287** 1019
[35] Ronning C, Gao P X, Ding Y, Wang Z L and Schwen D 2004 *Appl. Phys. Lett.* **84** 783
[36] Huang M H, Mao S, Feick H, Yan H Q, Wu Y Y, Kind H, Weber E, Russo R and Yang P D 2001 *Science* **292** 1897
[37] Arnold M S, Avouris Ph, Pan Z W and Wang Z L 2003 *J. Phys. Chem.* B **107** 659
[38] Cui Y and Lieber C M 2001 *Science* **291** 851
[39] Collins P G, Arnold M S and Avouris Ph 2001 *Science* **292** 706
[40] Kong J, Franklin N, Wu C, Pan S, Cho K J and Dai H 2000 *Science* **287** 622
[41] Avouris Ph 2002 *Chem. Phys.* **281** 429
[42] Advani G N, Kluge-Weiss P, Longini R L and Jordan A G 1980 *Int. J. Electron.* **48** 403
[43] Samson S and Fonstad C G 1973 *J. Appl. Phys.* **44** 4618
[44] Kamp B, Merkle R and Maier J 2001 *Sensors Actuators* B **77** 534
[45] Göpel W, Schierbaum K and Wiemhöfer H D 1989 *Solid State Ion.* **32** 440
[46] Mizusaki J, Koinuma H, Shimoyama J I, Kawasaki M and Fueki K 1990 *J. Solid State Chem.* **88** 443
[47] Zhang D H 1996 *Mater. Chem. Phys.* **45** 248
[48] Bonasewicz P, Hirschwald W and Neumann G 1986 *J. Electrochem. Soc.* **133** 2270
[49] Shapira Y, Cox S M and Lichtma D 1976 *Surf. Sci.* **54** 43
[50] Bai X, Wang E G, Gao P X and Wang Z L 2003 *Nano Lett.* **3** 1147
[51] Comini E, Faglia G, Sberveglieri G, Pan Z W and Wang Z L 2002 *Appl. Phys. Lett.* **81** 1869
[52] Kim P, Shi L, Majumdar A and McEuen P L 2001 *Phys. Rev. Lett.* **87** 215502
[53] Schwab K, Henriksen E A, Worlock J M and Roukes M L 2000 *Nature* **404** 974
[54] Shi L, Hao Q, Yu C, Kim D, Mingo N, Kong X Y and Wang Z L 2004 *Appl. Phys. Lett.* **84** 2638
[55] Volz S G and Chen G 1999 *Appl. Phys. Lett.* **75** 2056
[56] Sverdrup P G, Ju Y S and Goodson K E 2001 *J. Heat Transfer* **123** 130
[57] Poncharal P, Wang Z L, Ugarte D and de Heer W A 1999 *Science* **283** 1513
[58] Wang Z L, Poncharal P and de Heer W A 2000 *Pure Appl. Chem.* **72** 209
[59] Gao R P, Wang Z L, Bai Z G, de Heer W A, Dai L M and Gao M 2000 *Phys. Rev. Lett.* **85** 622
[60] Wang Z L, Dai Z R, Bai Z G, Gao R P and Gole J 2000 *Appl. Phys. Lett.* **77** 3349
[61] Meirovich L 1986 *Elements of Vibration Analysis* 2nd edn (New York: McGraw-Hill)
[62] Bai X D, Wang E G, Gao P X and Wang Z L 2003 *Appl. Phys. Lett.* **82** 4806
[63] Gao R P, Pan Z W and Wang Z L 2001 *Appl. Phys. Lett.* **78** 1757
[64] Bai X D, Wang E G, Gao P X and Wang Z L 2003 *Nano Lett.* **3** 1147
[65] Dai H J, Hafner J H, Rinzler A G, Colbert D T and Smalley R E 1996 *Nature* **384** 147
[66] Hughes W and Wang Z L 2003 *Appl. Phys. Lett.* **82** 2886
[67] Zhao M H, Wang Z L and Mao S X 2004 *Nano Lett.* **4** 587